Available online at www.sciencedirect.com
ScienceDirect
International Journal of Heat and Mass Transfer 50 (2007) 1865–1878
International Journal of HEAT and MASS TRANSFER
www.elsevier.com/locate/ijhmt

Numerical investigation of the influence of roughness on the laminar incompressible fluid flow through annular microchannels

José R. Valdés [a,*], Mario J. Miana [a], José Luis Pelegay [a], José Luis Núñez [a], Thomas Pütz [b]

[a] Instituto Tecnológico de Aragón, María de Luna 8, 50018 Zaragoza, Spain
[b] TRW Automotive, Carl-Spaeter Strasse 8, D-56070 Koblenz, Germany

Received 31 March 2006
Available online 28 November 2006

Abstract

The main objective of this work is to investigate, by means of numerical simulation, the effects of the surface roughness on the laminar fluid flow through annular microchannels, and to propose a method to take into account the surface roughness effects in the calculation or simulation of the fluid flow through these microchannels. This method is based on the classical viscous flow equations, and consists in building an equivalent smooth channel with the same flow resistance as the "rough" one.

Keywords: Fluid flow; Microchannels; Surface roughness; Numerical simulation

1. Introduction

The aim of this work is to investigate several aspects of the numerical simulation of fluid flow through microchannels. The motivation for this work is the simulation of seal systems, and in particular, the necessity to accurately calculate the flow rate that sometimes appears through the space that exists between a seal and the housing that contains it (see Fig. 1). Such case is sometimes found, among other applications, in the brake cylinder seals that separate the pressurized chamber and the chamber where the brake liquid is at atmospheric pressure. In some situations, these seals must allow the flow of liquid from one chamber to another, forming annular channels of very small width and length.

Due to the very small width of the channels that are formed in these seal systems, the roughness of the surfaces involved plays a non-negligible role. The aim of this piece of work is to analyse whether it is possible to derive a "simple" methodology to include the influence of roughness in the calculation of the flow rates that appear through these seal channels. For deriving this methodology, the classical viscous flow theory will be used. Therefore, the first part of this work is aimed at establishing the coherence between the classical theory applied to flows through very narrow channels and experimental results.

The equations of mass, energy and momentum conservation applied to a control volume of an incompressible fluid flowing through a duct of constant cross-sectional area lead to the Darcy–Weisbach equation for pressure drop [26]:

$$\Delta P = \frac{f \cdot \rho \cdot L \cdot V^2}{2 \cdot d_h} \tag{1}$$

where L is the duct length, V is the mean flow velocity, ρ is the fluid density, d_h is the hydraulic diameter and f is the friction factor. The last two are defined as

$$d_h = \frac{4 \cdot A}{P_{wet}} \tag{2a}$$

$$f = \frac{8 \cdot \tau_w}{\rho \cdot V^2} \tag{2b}$$

* Corresponding author. Tel.: +34 976 716211; fax: +34 976 716201.
E-mail address: jrvaldes@ita.es (J.R. Valdés).

0017-9310/$ - see front matter © 2006 Elsevier Ltd. All rights reserved.
doi:10.1016/j.ijheatmasstransfer.2006.10.006

Nomenclature

a	annular channel external radius
A	cross-sectional area
A_{efec}	average cross-sectional area
A_{wet}	channel surface in contact with the fluid
b	annular channel internal radius
d_h	hydraulic diameter
f	friction factor
$f \cdot Re$	Poiseuille number
H	average roughness peak height
K	flow resistance coefficient
L	length
P	static pressure
P_{wet}	channel perimeter in contact with the fluid
Q	volume flow
Re	Reynolds number
V	mean flow velocity
V_{fluid}	net volume occupied by the fluid

Greek symbols

ε	relative roughness $\varepsilon = h/d_h$
Δ	increment
μ	fluid viscosity
ρ	density
τ_w	wall shear stress
ξ	geometry coefficient of the friction factor

Subscripts

BC	between the inlet and outlet boundary conditions of the CFD model
Channel	between the initial and final sections of the microchannel region
Lin	linear losses
Min	minor losses
0.1 bar	results from case with 0.1 bar of ΔP between inlet and outlet boundary conditions
Eff	effective (including the effects of the minor losses)

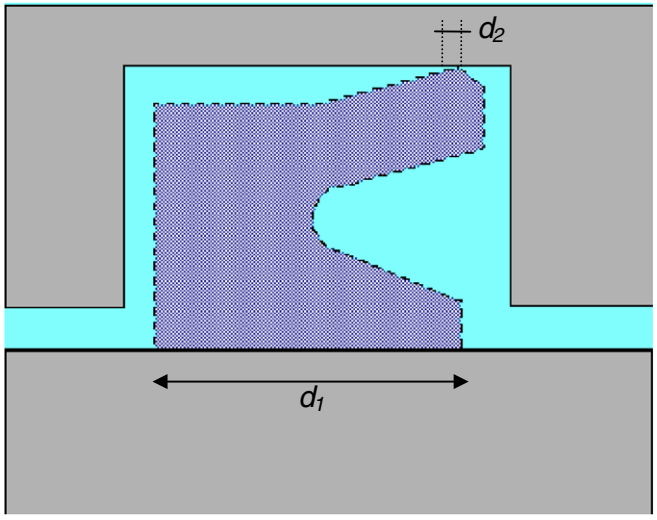

Fig. 1. Sketch of a typical seal system.

where A is the cross-sectional area of the channel, P_{wet} is the perimeter of the channel and τ_w is the wall shear stress. From dimensional analysis, it can be shown that the friction factor depends on the Reynolds number:

$$Re = \frac{\rho \cdot V \cdot d_h}{\mu} \tag{3}$$

where μ is the fluid viscosity.

Solving the conservation equations for laminar flow, an exact solution of the velocity profile can be obtained. This type of flow is called Hagen–Poiseuille flow, and the resulting value of the friction factor for this type of flow is

$$f = 64/Re \tag{4}$$

for circular ducts, and

$$f = 64\xi/Re \tag{5a}$$

for annular ducts, with

$$\xi = \frac{(a-b)^2 \cdot (a^2-b^2)}{\left[a^4 - b^4 - \left(a^2-b^2\right)^2\right] \cdot \ln\left(\frac{a}{b}\right)} \tag{5b}$$

where a and b are the external and internal radii of the tube, respectively [26].

In general, for fully developed flows in ducts of constant cross-section, a relationship of the form $f \cdot Re = C$ exists, where C is a constant dependent only on the channel geometry (64 for circular ducts, 64ξ for annular ducts, etc). The usual approach of most numerical and experimental studies is to obtain f and Re and compare the resulting value of the Poiseuille number with the corresponding value obtained from the macroscale flow theory.

For annular ducts, the pressure drop can be calculated as

$$\Delta P = K \cdot Q \tag{6}$$

$$Q = A \cdot V \tag{7}$$

where Q is the volume flow and

$$K = \frac{32 \cdot \xi \cdot \mu \cdot L}{A \cdot d_h^2} \tag{8}$$

is the flow resistance coefficient, which only depends on the geometry of the channel and the viscosity of the fluid.

The available research papers on laminar flow through microchannels can be roughly classified into two categories: those that report that the measured flow exhibits a significantly different pressure drop from that predicted by the classical theory [1–12] and those that report a consistent behaviour between experiments, simulations and the classical theory [13–23]. Most of the articles falling into the first category were published before the year 2000, while the more recent papers tend to show consistency between theory, experiments and simulation.

The more detailed experiments performed during the last years show that the laminar flows through microchannels are consistent with the classical theories and that the deviations that appeared in previous papers are probably due to measurement uncertainties, errors in the diameter measurements, instrumentation errors, failure to consider other pressure losses present in the experiments, etc. In particular, the results reported in [19] suggest that friction factors for microchannels with hydraulic diameters ranging between 25 and 100 μm and *Re* numbers between 5 and 2068 can be accurately determined from the classical theory. In this study, the internal pressure measurements were corrected to represent only the pressure drop inside the channel, by subtracting other pressure drops of the experimental setup, such as the losses due to changes in tubing diameters, bends, tees, and the pressure drop associated with the developing flow in the entrance region of the channel. The agreement between the experimental and the predicted results was excellent for all tested channels.

Finite volume calculations of laminar flow in microchannels performed in [20] report that the friction factors obtained in the numerical calculations are consistent with the theoretical values. The experiments of Xu et al. [14], who considered liquid flow in 30–344 μm diameter channels at *Re* numbers between 20 and 4000, showed that the characteristics of flow in microchannels agree with the conventional behaviour predicted by the Navier–Stokes equations. Furthermore, they showed that the only deviations they found were due to dimensional measurement errors during the experiments.

Judy et al. [16] made extensive frictional pressure drop measurements for *Re* numbers between 8 and 2300 in 15–150 μm diameter microtubes and no significant deviation from the macroscale flow theory was found.

Research papers also report roughness effects as a cause for deviations from macroscale theory [10,24,25], associating with them an increase in Poiseuille number with respect to conventional theory. Croce and D'Agaro [25] investigated effects of roughness on flow through microchannels by means of CFD simulations, detecting a significant increase in the Poiseuille number for all configurations studied (relative roughness ε between 0.5% and 5.3%, where ε is defined as the ratio between the average roughness peak height h and the channel diameter). Some authors [10,24] propose a roughness viscosity model to account for the effects of the surface roughness, which requires an experimentally determined coefficient. Xu et al. state in [14] that effects of the surface roughness can be neglected when $\varepsilon < 3\%$. Results of [14,19] are in agreement with this observation, since the roughness of the tested ducts was lower than 3% and no deviations due to roughness were found.

2. Laminar incompressible flow through annular microchannels

In part 3, the studies about the influence of roughness upon the flow through very short and very narrow annular tubes will be based on the comparison of the flow resistance results from numerical simulations with values calculated with the classical viscous flow theory. Therefore, before undertaking this part of the investigation, it is interesting to check that, for smooth channels, the numerical simulations provide results that are coherent with the theory and, therefore, with the experimental measurements, as most of the recent research papers show an excellent correlation between the experimental measurements of fluid flow in microchannels and the analytically predicted solutions. In this way, when comparing the simulation results in rough channels with the theoretical results in smooth channels, the differences will surely be due to the effects of roughness.

In order to perform such analysis, CFD models of simple annular tubes of different hydraulic diameters and lengths, with different pressure drops between inlet and outlet, have been built and solved, in order to have results over a wide range of laminar Reynolds numbers. All the cases that have been solved are well below *Re* 2300, the accepted value for transition to turbulent flow.

Fig. 2 shows the geometry of the annular microchannels that have been simulated and Table 1 shows a summary of the different cases that have been solved. The first length value, 2.8 mm, is a typical value of the contact length of a seal designed for separating two chambers (dimension d_1 in Fig. 1). However, in some situations, the seal might be separated from the housing, allowing the formation of a microchannel through which the leakage flow must be evaluated. The other value, 0.1 mm, is an extremely short value that can be typical of seal lips that, at given situations, must collapse to allow the flow of liquid from

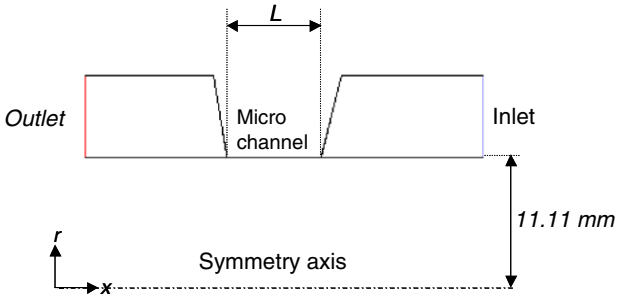

Fig. 2. Geometry of the annular microchannel model (*L* indicates the microchannel length).

Table 1
Simulated cases

ΔP_{BC}	L=2.8 mm; d_h=100 μm; a=11.16 mm; b=11.11 mm	L=2.8 mm; d_h=20 μm; a=11.12 mm b=11.11 mm	L=0.1 mm; d_h=20 μm; a=11.12 mm b=11.11 mm
0.1 bar			
0.2 bar			
0.3 bar			
0.5 bar			
1 bar			
5 bar			
10 bar			
50 bar			
100 bar			

one side to the other (dimension d_2 in Fig. 1). The gap width values, 20 and 100 μm, have been selected to represent two possible situations in these type of systems.

Since our main motivation is the flow through very narrow channels in seal systems, and, in particular, in brake cylinder seals, a typical brake oil has been modelled (see properties in Table 2).

The domain is 2D axisymmetric. An inlet pressure boundary condition has been specified at the right side of the model and an outlet pressure boundary condition has been imposed at the other end. At the outlet pressure boundary, a constant static pressure of 0 Pa relative to the atmospheric pressure is set, while at the inlet boundary, different total pressure levels are imposed, from 0.1 to 100 bar. At inlet pressure boundary conditions, total pressure (static plus dynamic pressure) values must be used: that is why a large fluid volume is allowed at the right side of the microchannel, so that the total pressure at the inlet BC coincides with the static pressure. The area of the inlet BC must be large enough to make negligible the dynamic pressure at the inlet BC. At the model outlet region, another fluid volume has been allowed in order to move the outlet BC of the model away from the channel outlet. At the rest of the model boundaries a non-slip wall boundary condition is imposed. The entrance and exit of the channel is a little tapered, just to somehow resemble the geometry of the upper lip channel of Fig. 1.

The following continuity and momentum equations are solved by means of the finite volume method using the segregated implicit double precision solver of the commercial code FLUENT [27] assuming the hypotheses of laminar steady-state, incompressible two dimensional axisymmetric isothermal flow of a Newtonian fluid:

$$\frac{1}{r}\frac{\partial}{\partial r}(rv_r)+\frac{\partial}{\partial z}(v_z)=0 \tag{9}$$

$$v_r\frac{\partial v_r}{\partial r}+v_z\frac{\partial v_r}{\partial z}=-\frac{1}{\rho}\frac{\partial P}{\partial r}+\nu\left[\frac{\partial}{\partial r}\left(\frac{1}{r}\frac{\partial}{\partial r}(rv_r)\right)+\frac{\partial^2 v_r}{\partial z^2}\right]+g_r \tag{10}$$

$$v_r\frac{\partial v_z}{\partial r}+v_z\frac{\partial v_z}{\partial z}=-\frac{1}{\rho}\frac{\partial P}{\partial z}+\nu\left[\frac{1}{r}\frac{\partial}{\partial r}\left(r\frac{\partial v_z}{\partial r}\right)+\frac{\partial^2 v_z}{\partial z^2}\right]+g_z \tag{11}$$

Double precision is required to accurately capture the small grid dimensions, areas and volumes. A point implicit (Gauss–Seidel) linear equation solver is used in conjunction with an algebraic multigrid (AMG) method to solve the resultant scalar system of equations for the dependent variable in each cell.

A co-located scheme is used for the storage of the pressure and velocity variables at the centre of each cell. The convective term of the momentum equation is calculated from the face values, which are calculated from the cell values by means of second order upwind schemes.

The momentum and continuity equations are solved sequentially. The continuity equation is used as an equation for pressure, but pressure does not appear explicitly in the continuity equation for incompressible flows, since density is not directly related to pressure. The SIMPLE [28] (semi-implicit method for pressure-linked equations) algorithm is used for introducing pressure into the continuity equation. A detailed description of the numerical methods included in FLUENT can be found in Mathur and Murthy [29] or Kim et al. [30].

Table 2
Fluid properties

	−30 °C	23 °C
ρ (kg/m^3)	1100	1057
μ (kg/m s)	0.4900	0.0134

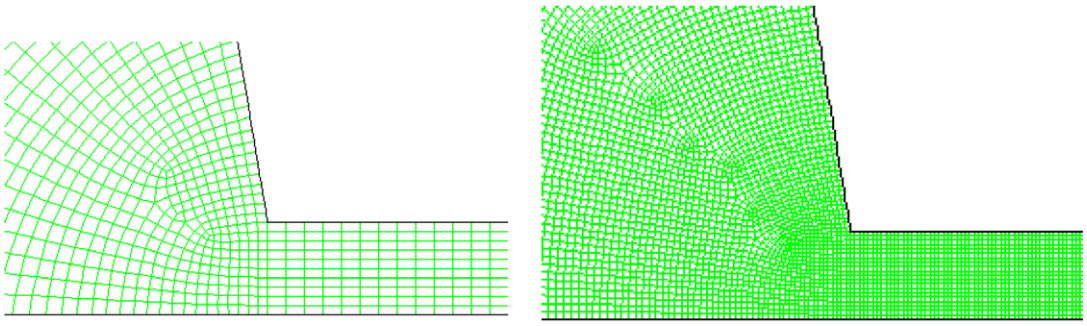

Fig. 3. Mesh detail of the annular microchannel model: initial mesh (left), refined mesh (right).

A fine mesh with 10 cells across the channel is built. A refined mesh with twice the number of cells across the channel region and a strong refinement in the channel inlet and outlet regions is also built (Fig. 3). The difference between the Poiseuille number values yielded by both grids is only 1.5% (see Table 3), which shows a high degree of grid independence. The refined mesh is then used for running all the cases of this study. As it will be remarked below, the results of this mesh only differ from the theoretical ones in 0.5%, which indicates a very good agreement. The initial mesh has approximately 12,300 cells, while the refined one has about 31,000 cells.

The indicator of calculation convergence is the scaled residual for each of the conserved variables (see [27]), the mass flow imbalance throughout the domain and the mass flow stability along the calculation. In particular, the simulation is considered to be converged when each of the residuals is below 1e−12, the mass flow imbalance is four orders of magnitude smaller than the average mass flow rate value and the change in mass flow rate from one iteration to the next is at least four orders of magnitude smaller than the average mass flow rate through the domain.

The CFD simulation provides the resulting volume flow for each case, the mean velocity is calculated from Eq. (7), the Reynolds number is calculated from Eq. (3), the friction factor is calculated from Eq. (1), and from these two the Poiseuille number is calculated. In Eq. (1), ΔP represents the pressure drop inside the channel. Therefore, from now on, $\Delta P_{\text{channel}}$ will refer to the pressure difference between the initial and final sections of the microtube and ΔP_{BC} will refer to the pressure difference imposed between the inlet and outlet boundary conditions of the CFD model. $\Delta P_{\text{channel}}$ does not take into account either the pressure losses upstream the tube inlet due to the contraction or the losses downstream the tube outlet due to the expansion, and it is the value that has to be used when applying Eq. (1). The resistance coefficient K is computed from Eq. (6). The theoretical Poiseuille number is computed from Eq. (5a), being the value of $\xi = 1.5$ for all the tubes that have been simulated, where ξ is the geometrical parameter defined in Eq. (5b). Results are summarised in Table 4.

Table 3
Initial mesh and refined mesh results

d_h (mm)	L (mm)	ΔP_{BC} (bar)	Initial mesh, 12,300 cells $f \cdot Re$	Refined mesh, 31,000 cells $f \cdot Re$	Difference (%)
100	2.8	0.1	94.16	95.60	1.53
100	2.8	100	98.57	99.64	1.09
20	2.8	0.1	94.12	95.55	1.52
20	2.8	100	94.13	95.54	1.50
20	0.1	0.1	94.81	96.27	1.54
20	0.1	100	98.23	99.32	1.11

The numerical results match very well the theoretical ones (less than 1.5% difference), except for high pressure drop conditions (more than 50 bar), where the numerical results depart from the theoretical value, due to the secondary losses associated with the flow developing and the sharp area contraction. The linear flow resistance coefficient K of the microchannel can be found, using Eq. (6), from the cases in which $\Delta P_{\text{BC}} = 0.1$ bar, where there are practically no minor pressure losses and the length of the fully developed region coincides with the length of the channel. This assumption is supported by the fact that in the cases in which $\Delta P_{\text{BC}} = 0.1$ bar, the velocity profile is already developed at the entrance of the tube (Fig. 4), the pressure drop along the channel is linear (Fig. 5) and the difference between the numerical and theoretical results is less than 0.5% (Table 4).

Then, for each pressure case, the minor or secondary pressure drop ΔP_{min} can be found as

$$\Delta P_{\text{min}} = \Delta P_{\text{channel}} - \Delta P_{\text{lin}} = \Delta P_{\text{channel}} - K \cdot Q \tag{12}$$

ΔP_{min} approximately represents the part of the pressure drop that is not linear (see Fig. 6 and Table 5). According to [19], the equation for the minor pressure losses has the form

$$\Delta P_{\text{min}} = 0.5 \cdot K_{\text{min}} \cdot \rho \cdot V^2 \tag{13}$$

from which the loss coefficient associated with the minor losses K_{min} can be calculated (Table 5):

$$K_{\text{min}} = \Delta P_{\text{min}} \cdot 2 \cdot A^2/(\rho \cdot Q^2) \tag{14}$$

It can thus be concluded that the predicted CFD results (Table 4, cases of ΔP_{BC}=0.1 bar) agree very well with the expected theoretical results and are therefore coherent with the recent experiments that can be found in the

Table 4
CFD simulation results and comparison with theoretical results

d_h (mm)	L (mm)	ΔP_{BC} (bar)	$\Delta P_{channel}$ (bar)	Q (m^3/s)	Re	$f \cdot Re$ (CFD)	$f \cdot Re$ (theory)	Difference (%)
100	2.8	0.1	0.10	1.91E−07	0.43	95.60	96	−0.42
100	2.8	1	0.98	1.91E−06	4.30	95.60	96	−0.41
100	2.8	10	9.65	1.88E−05	42.36	95.79	96	−0.22
100	2.8	50	44.67	8.55E−05	192.77	97.46	96	1.52
100	2.8	100	83.32	1.56E−04	351.74	99.64	96	3.79
100	2.8	200	151.24	2.72E−04	614.25	103.57	96	7.88
20	2.8	0.1	0.10	1.55E−09	0.00	95.55	96	−0.47
20	2.8	1	1.00	1.55E−08	0.04	95.54	96	−0.48
20	2.8	5	4.98	7.76E−08	0.18	95.54	96	−0.48
20	2.8	10	9.96	1.55E−07	0.35	95.54	96	−0.48
20	2.8	100	99.57	1.55E−06	3.51	95.54	96	−0.48
20	0.1	0.1	0.09	3.87E−08	0.09	96.27	96	0.28
20	0.1	1	0.89	3.87E−07	0.87	96.27	96	0.28
20	0.1	10	8.90	3.85E−06	8.71	96.32	96	0.33
20	0.1	50	42.04	1.80E−05	40.65	97.44	96	1.50
20	0.1	100	77.88	3.27E−05	73.88	99.32	96	3.46
20	0.1	200	140.07	5.61E−05	126.80	104.09	96	8.42
20	0.1	400	246.52	9.38E−05	212.06	109.53	96	14.10
20	0.1	800	429.57	1.49E−04	337.41	119.96	96	24.95

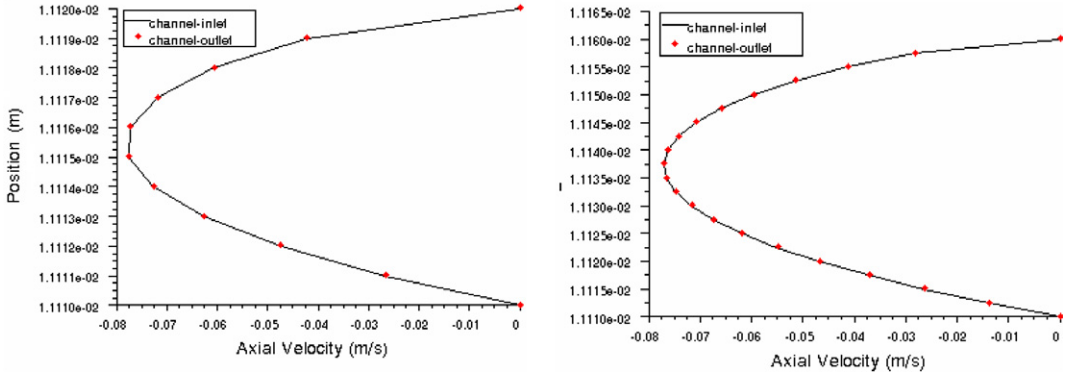

Fig. 4. Axial velocity profiles at the inlet and outlet of the microchannel for $\Delta P = 0.1$ bar; $d_h = 20$ μm, $L = 0.1$ mm (left) and $d_h = 100$ μm, $L = 2.8$ mm (right).

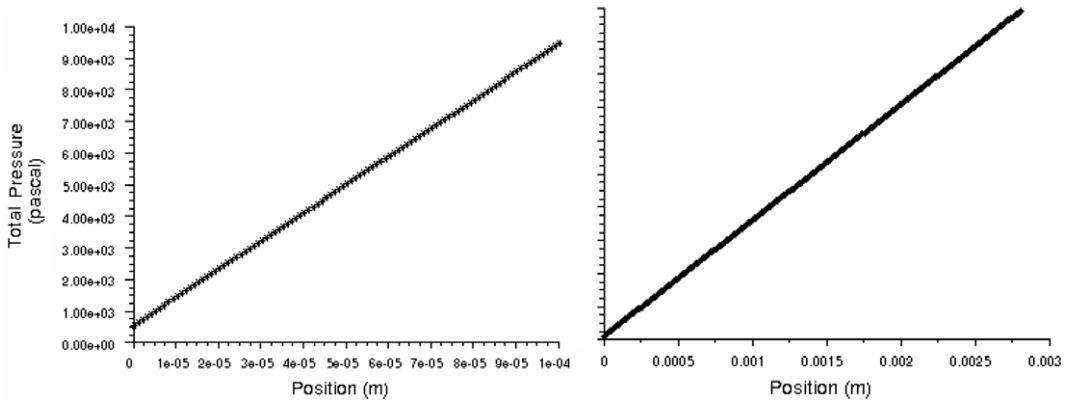

Fig. 5. Pressure drop along the channel for $\Delta P = 0.1$ bar; $d_h = 20$ μm, $L = 0.1$ mm (left) and $d_h = 100$ μm, $L = 2.8$ mm (right).

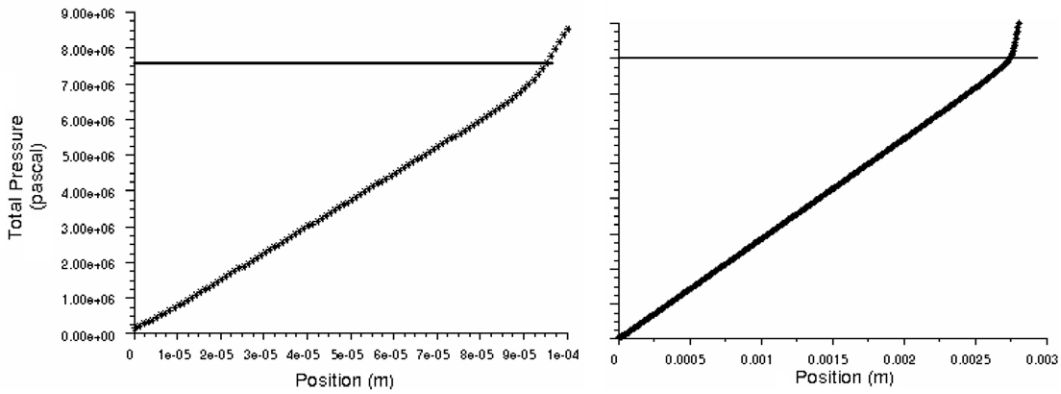

Fig. 6. Pressure drop along the channel for $\Delta P = 100$ bar; $d_h = 20$ μm, $L = 0.1$ mm (left) and $d_h = 100$ μm, $L = 2.8$ mm (right). The straight line indicates the approximate value (Table 5) of the linear pressure drop $\Delta P_{lin} = K \cdot Q$.

Table 5
Results of ΔP_{min} and K_{min}

d_h (mm)	L (mm)	ΔP_{BC} (bar)	ΔP_{lin} (bar)	ΔP_{min} (bar)	K_{min}
100	2.8	0.1	0.10	0.00	0.00
100	2.8	1	0.98	0.00	0.05
100	2.8	10	9.63	0.02	0.12
100	2.8	50	43.81	0.86	0.27
100	2.8	100	79.94	3.38	0.32
100	2.8	200	139.60	11.64	0.36
20	2.8	0.1	0.10	0.00	0.00
20	2.8	1	1.00	0.00	0.00
20	2.8	5	4.98	0.00	0.00
20	2.8	10	9.96	0.00	0.00
20	2.8	100	99.56	0.01	0.00
20	0.1	0.1	0.09	0.00	0.00
20	0.1	1	0.89	0.00	0.00
20	0.1	10	8.89	0.00	0.03
20	0.1	50	41.54	0.50	0.14
20	0.1	100	75.49	2.39	0.21
20	0.1	200	129.56	10.52	0.31
20	0.1	400	216.67	29.85	0.31
20	0.1	800	344.75	84.82	0.35

bibliography. As a general rule, for *Re* numbers greater than 50, the pressure drop associated with the developing flow and other minor losses should be taken into account.

3. Analysis of the influence of roughness

The agreement between the numerical simulations of the flow through short and narrow microchannels and the classical viscous flow theory has been demonstrated in the previous section. In this section the numerical approach will be used to analyse the effect of the wall roughness on the fluid flow. Following the approach undertaken by [25], the roughness is simulated by the superimposition of randomly generated triangular peaks on the inner wall of a smooth microchannel. Since the model is axisymmetric, the modelled peaks are not representative of the real imperfections present in the material, but will be useful to analyse their effects on the fluid flow.

Six different models have been built and run, in order to compare the resulting flow resistance coefficients and Poiseuille numbers with the respective values of the corresponding original smooth tube (without the peaks). These models are shown in Fig. 7 and their main characteristics are shown in Table 6. The channel of length 0.1 mm with hydraulic diameters of 10 and 20 μm is selected for this analysis, mainly because in this initial study we are particularly interested in the flow through very short channels, such as the one formed by the upper lip of the seal and the wall in Fig. 1. Simulations have been run only for very low *Re* number values (pressure drops up to 10 bar), where the minor losses can be neglected.

The six roughness models that have been implemented have different values of average peak height, relative roughness and peak density. Models 1 and 2 have a similar, very low peak density with a sharp increase in peak height and relative roughness in model 2 with respect to model 1. Models 2 and 3 have a similar average peak height and relative roughness, and an abrupt increase in peak density in model 3 with respect to model 2. Models 3–6 have the same peak density and different relative roughness, which is increased from model 3 to model 6 either by increasing the peak height or decreasing the hydraulic diameter. This is an initial study where the global influence of roughness and the feasibility of developing an analytical model for calculating the flow through microchannels with rough walls is to be checked. Next steps to this work will include models with longer channel length values and more detailed parametric studies on peak density, average peak height and relative roughness.

The models are meshed with a fine grid of 20 elements across the channel. For each model, a study is conducted in order to establish grid independence. This is done by successively refining the mesh until the mass flow rate values (see Table 7) and the velocity results do not change significantly (see Fig. 9). The mesh is refined by adapting the regions where high velocity gradients are detected (see Fig. 8). For the first three models the initial mesh is adequate, while for the second three models one refinement

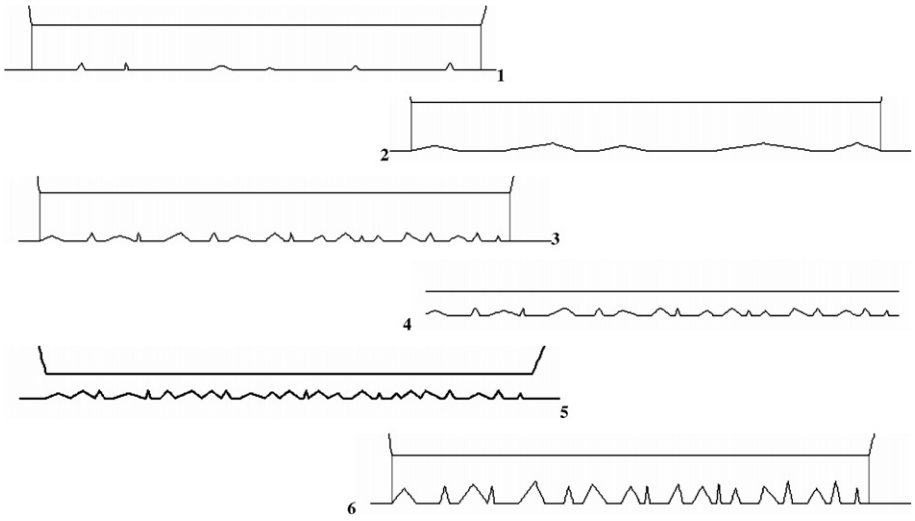

Fig. 7. Sketch of the microchannel models with different wall roughness (see Table 6 for the geometric dimensions of each channel).

Table 6
Main features of the models with wall roughness

	Max. peak height (μm)	Average peak height h (μm)	Hydraulic diameter d_h (μm)	Relative roughness $\varepsilon = h/d_h$ (%)	Peak density (number of peaks/mm)	Internal radius (mm)	External radius (mm)	Length (mm)
Model 1	1.5	0.120	20	0.60	60	11.110	11.120	0.1
Model 2	1.5	0.435	20	2.18	50	11.110	11.120	0.1
Model 3	1.5	0.401	20	2.00	180	11.110	11.120	0.1
Model 4	1.5	0.401	10	4.00	180	11.110	11.115	0.1
Model 5	1.5	0.550	10	5.50	180	11.110	11.115	0.1
Model 6	4	1.420	20	7.10	180	11.110	11.120	0.1

Table 7
Grid refinement study

	Model 1	Model 2	Model 3	Model 4	Model 5	Model 6
$\Delta P_{BC} = 0.1$ bar						
Initial mesh	3.81E−05	3.52E−05	3.32E−05	3.52E−06	3.15E−06	1.46E−05
Refined mesh 1	3.77E−05	3.50E−05	3.26E−05	3.30E−06	2.93E−06	1.38E−05
Difference (%)	−1.2	−0.6	−1.7	−6.1	−7.0	−5.3
Refined mesh 2				3.32E−06	2.93E−06	1.39E−05
Difference (%)				0.6	0.1	0.6
$\Delta P_{BC} = 10$ bar						
Initial mesh	3.76E−03	3.50E−03	3.26E−03	3.50E−04	3.14E−04	1.44E−03
Refined mesh 1	3.73E−03	3.48E−03	3.26E−03	3.30E−04	2.93E−04	1.38E−03
Difference (%)	−0.7	−0.4	0.0	−5.7	−6.7	−4.1
Refined mesh 2				3.29E−04	2.93E−04	1.37E−03
Difference (%)				−0.3	−0.1	−0.7
Final no. of cells	19,200	19,070	19,080	51,070	49,350	119,360

Mass flow rates (kg/s) for the different meshes built for each model and % difference between each mesh and the following refinement.

is necessary (see Table 7). The number of elements of the final grid used for each model is also shown in Table 7.

From the CFD simulations, the resulting values of the flow resistance coefficient K and the Poiseuille number $f \cdot Re$ can be compared with those of the corresponding smooth channel. Results are shown in Table 8.

The results confirm the trends indicated by other research papers, that show a significant increase of the friction factor and the Poiseuille number with roughness, even for small roughness values. This is logical, since the wall roughness reduces the available cross-sectional area and increases the wall surface in contact with the fluid, therefore decreasing the hydraulic diameter (see Fig. 9). All these facts tend to increase the friction factor and the pressure drop.

The deviations from the macroscale theory increase as the value of the relative roughness parameter increases. From models 2 and 3, it can also be noted that the density

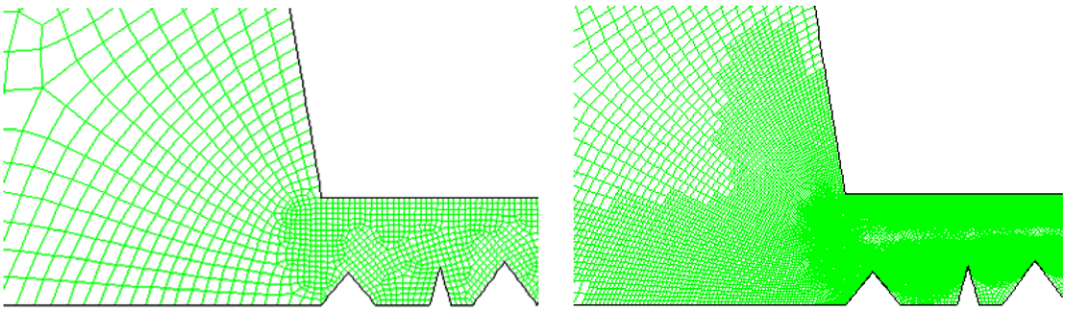

Fig. 8. Detail of the mesh of model 6: initial (left), refined (right).

Table 8a
Poiseuille number $f \cdot Re$

ΔP_{BC} (bar)	$f \cdot Re$ smooth	$f \cdot Re$ model 1	$f \cdot Re$ model 2	$f \cdot Re$ model 3	$f \cdot Re$ model 4	$f \cdot Re$ model 5	$f \cdot Re$ model 6
0.1	96.00	104.44	114.10	124.38	161.27	182.37	308.55
0.5	96.00	104.48	114.13	124.36	161.27	181.77	307.70
1	96.00	104.54	114.16	124.38	161.27	182.39	308.60
5	96.00	105.06	114.45	124.36	161.27	181.76	307.70
10	96.00	105.77	114.89	124.38	161.27	182.38	308.60

Results from the six CFD models and theoretical value of the microchannel without roughness.

Table 8b
Increase of the Poiseuille number due to roughness

ΔP (bar)	Model 1	Model 2	Model 3	Model 4	Model 5	Model 6
0.1	8.84%	18.92%	29.63%	68.07%	90.06%	221.57%
0.5	8.89%	18.94%	29.60%	68.08%	89.44%	220.68%
1	8.96%	18.98%	29.63%	68.08%	90.08%	221.62%
5	9.49%	19.28%	29.60%	68.08%	89.43%	220.68%
10	10.23%	19.74%	29.63%	68.07%	90.08%	221.62%

of peaks has a certain influence. Model 3 has a slightly lower value of ε than model 2, but, due to the significantly higher density of peaks, the Poiseuille number is also significantly higher.

Fig. 9 shows a reduction of available area and an increase of the thickness of the boundary layer. Clearly, a macroscale theory that uses the same parameters as for a smooth tube cannot be applied in this case. Some parameters must be modified in order to take into account the influence of the peaks. Some authors propose the use of a modified viscosity model, which is not simple and requires experimentally adjusted coefficients. Here we propose a simpler approach, which consists in modifying some geometrical parameters.

Approach 1. The first approach consists in analysing the possibility of simulating the roughness effect by means of an equivalent smooth microchannel with the same fluid volume (or average cross-sectional area) as the rough one. In order to do that, one of the radii must be modified so as to provide a smooth channel with the same fluid volume as the rough one. In the CFD models, the fluid volume is directly calculated by the CFD code. In real cases, the fluid volume should be estimated from the relative roughness parameter ε or the mean peak height or from scanning probe microscopy images [31]. This poses a new and different challenge in itself, and should be treated in a different research work.

The modified radius b' is calculated so as to have the same volume (or average cross-section) as the rough channel:

$$A_{efec} = \frac{V_{fluid}}{L} = \pi \cdot (a^2 - b'^2)$$
$$b' = \sqrt{a^2 - \frac{V_{fluid}}{L \cdot \pi}} \tag{15}$$

The flow resistance coefficient K of each rough channel is compared with that of its equivalent smooth channel. CFD simulations can be run for the equivalent smooth channels, but as demonstrated in Section 2, the value of the resistance provided by the macroscale theory is accurate enough, being the difference between the CFD result and the analytical value less than 2%. Table 9 shows the difference between the resistance of the rough channels (CFD simulations) and the resistance (Eq. (8)) of the equivalent smooth channels with modified radii.

Only for the first two models are the differences below 10%. The errors are smallest in model 2, which has higher relative roughness and slightly lower peak density than

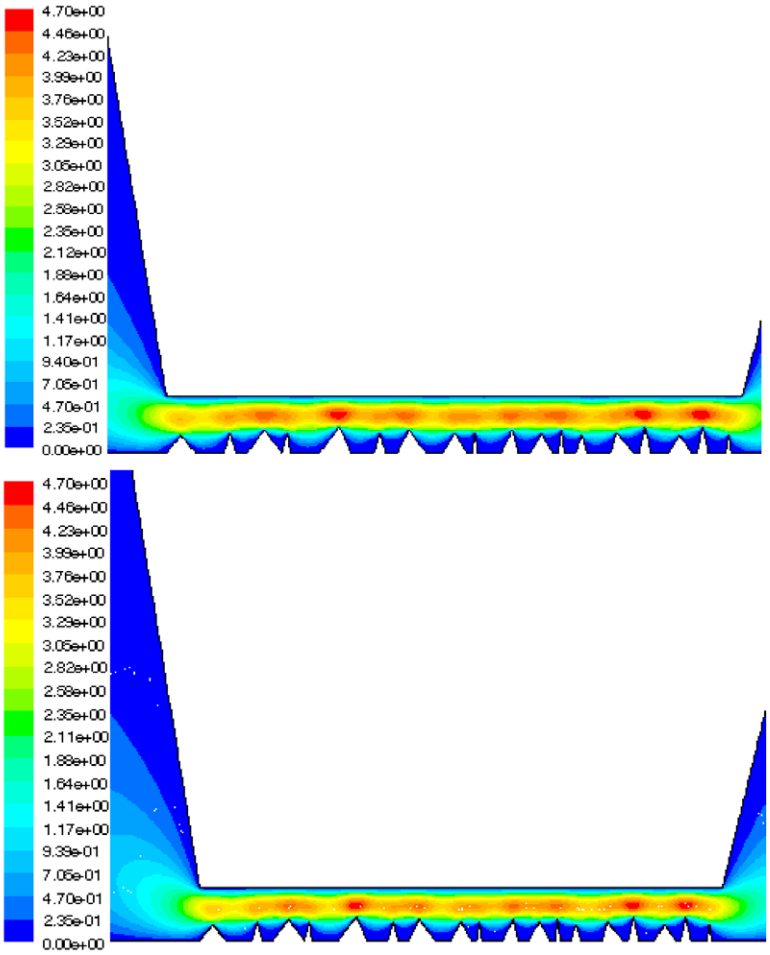

Fig. 9. Velocity (m/s) contours for model 6 with ΔP 10 bar: initial mesh (top) and refined mesh (bottom).

Table 9
Difference between the flow resistance coefficient K of the equivalent smooth channel (Approach 1) with respect to the actual flow resistance coefficient K of the corresponding rough channel (obtained from the CFD simulations)

	Model 1	Model 2	Model 3	Model 4	Model 5	Model 6
23 °C						
K equivalent	2.36E+11	2.63E+11	2.56E+11	2.28E+12	2.54E+12	3.18E+11
0.1 bar	−5.95%	−3.84%	−14.40%	−26.37%	−27.46%	−57.10%
0.5 bar	−5.99%	−3.86%	−14.38%	−26.37%	−27.23%	−56.99%
1 bar	−6.05%	−3.89%	−14.40%	−26.37%	−27.47%	−57.11%
5 bar	−6.51%	−4.13%	−14.38%	−26.37%	−27.22%	−56.99%
10 bar	−7.13%	−4.50%	−14.40%	−26.37%	−27.47%	−57.11%
−30 °C						
K equivalent	8.62E+12	9.63E+12	9.34E+12	8.33E+13	9.30E+13	1.16E+13
0.1 bar	−5.91%	−3.76%	−12.25%	−26.36%	−27.38%	−57.92%
0.5 bar	−5.94%	−3.77%	−12.26%	−26.36%	−27.38%	−57.99%
1 bar	−5.99%	−3.77%	−12.26%	−26.36%	−27.38%	−58.01%
5 bar	−5.94%	−3.77%	−12.26%	−26.36%	−27.38%	−58.52%
10 bar	−5.99%	−3.77%	−12.26%	−26.36%	−27.38%	−58.02%

model 1, and similar relative roughness as model 3, but much lower peak density. This indicates that, in this approach, the influence of peak density is significant. As the relative roughness and peak density increases, this equivalent-volume model seems to fail. Looking at the velocity contours (Fig. 9), it is clear that a space much larger than the volume occupied by the roughness peaks is being "not used" by the flow. It looks as if a value directly related with the peak height should be a much more influential parameter in the flow pattern.

Approach 2. Following the last conclusion, the first logical trial is to modify the value of the inner radius by adding to it the peak height average or RMS value. The resistance of the smooth channel obtained in this way is compared with that of its corresponding rough channel.

The modification of the inner radius by adding the average peak height gives similar results as the previous approach (see Table 10), except in the high roughness cases, where it is even worse. It can be shown that, in fact, both approaches are similar. If we assume that the fluid volume of the smooth channel built by adding to the inner radius the value of the peak height average is approximately

$$V_{\text{fluid}} = \pi \cdot \left(a^2 - (b+h)^2\right) \cdot L \tag{16}$$

Substituting this in Eq. (15), it results in $b' = b + h$, which is exactly the same as adding the average peak height to the radius.

Using the RMS value improves the results in all cases, making the errors smaller than 10% for models 1–3 (low relative roughness) both at room and low temperature. For the rest of the models, errors increase as the relative roughness increases (see Table 10).

Approach 3. The third approach consists in calculating an equivalent smooth channel with the same effective hydraulic diameter as the rough channel, defined as the ratio between the actual volume occupied by the fluid and the surface area in contact by the fluid, instead of the ratio between the cross-sectional area and the wet perimeter:

$$d_{\text{h}} = \frac{4V_{\text{fluid}}}{A_{\text{wet}}} \tag{17}$$

The flow resistance coefficient of the equivalent smooth channel is then calculated by means of Eq. (8). In the case of the CFD models, V_{fluid} and A_{wet} can be calculated by the very CFD code; however, in real cases, they should be estimated in another way; for example, using microscope measurements.

The flow resistance coefficient obtained with the CFD code can then be compared with the one calculated analytically in the equivalent smooth channel. Results are shown in Table 11.

At room temperature, the error is below 12% for the first five models and below 15% for the sixth model. At low temperature, the error is similar for the low roughness models (1–3) and increases in about 5 points for the models

Table 10
Difference between the flow resistance coefficient K of the equivalent smooth channel (Approach 2) with respect to the actual flow resistance coefficient K of the corresponding rough channel (obtained from the CFD simulations). For each model, the error value is very similar for all the ΔP_{BC} studied; the table shows the approximate average values obtained for each model

	Model 1	Model 2	Model 3	Model 4	Model 5	Model 6
23 °C						
Average peak height (μm)	0.120	0.435	0.401	0.401	0.550	1.420
Difference (%)	−5	−4	−14	−31	−34	−100
RMS peak height (μm)	0.327	0.636	0.608	0.608	0.722	1.900
Difference (%)	1	2	−8	−14	−19	−71
−30 °C						
Average peak height (μm)	0.120	0.435	0.401	0.401	0.550	1.420
Difference (%)	−5	−4	−12	−30	−34	−107
RMS peak height (μm)	0.327	0.636	0.608	0.608	0.722	1.900
Difference (%)	−2	−2	−5	−14	−19	−75

Table 11
Difference between the flow resistance coefficient K of the equivalent smooth channel (Approach 3) with respect to the actual flow resistance coefficient K of the corresponding rough channel (obtained from the CFD simulations)

	Model 1	Model 2	Model 3	Model 4	Model 5	Model 6
23 °C						
K equivalent	2.50E+11	2.55E+11	2.99E+11	2.58E+12	2.92E+12	6.03E+11
0.1 bar	−0.24%	−6.87%	2.25%	−11.17%	−9.99%	−13.94%
0.5 bar	−0.29%	−6.89%	2.18%	−11.15%	−10.04%	−13.98%
1 bar	−0.35%	−6.92%	2.10%	−11.17%	−9.98%	−14.04%
5 bar	−0.84%	−7.15%	1.41%	−11.30%	−10.27%	−14.49%
10 bar	−1.50%	−7.51%	0.53%	−11.56%	−10.27%	−15.08%
−30 °C						
K equivalent	9.15E+12	9.33E+12	1.09E+13	9.42E+13	1.07E+14	2.21E+13
0.1 bar	−0.11%	−6.74%	2.81%	−16.71%	−16.53%	−20.07%
0.5 bar	−0.13%	−6.74%	2.81%	−16.71%	−16.53%	−20.21%
1 bar	−0.19%	−6.74%	2.81%	−16.72%	−16.53%	−20.25%
5 bar	−0.13%	−6.74%	2.81%	−16.71%	−16.52%	−21.22%
10 bar	−0.19%	−6.74%	2.81%	−16.72%	−16.53%	−20.27%

Table 12
Difference between the flow resistance coefficient K of the equivalent smooth channel (Approach 4) with respect to the actual flow resistance coefficient K of the corresponding rough channel (obtained from the CFD simulations)

	Model 1	Model 2	Model 3	Model 4	Model 5	Model 6
23 °C						
K equivalent	2.52E+11	2.67E+11	3.10E+11	2.76E+12	3.25E+12	6.71E+11
0.1 bar	0.56%	−2.49%	5.80%	−4.72%	0.17%	−4.25%
0.5 bar	0.51%	−2.51%	5.73%	−4.70%	0.11%	−4.30%
1 bar	0.45%	−2.53%	5.64%	−4.72%	0.18%	−4.36%
5 bar	−0.04%	−2.78%	4.93%	−4.86%	−0.14%	−4.87%
10 bar	−0.71%	−3.16%	4.02%	−5.14%	−0.14%	−5.52%
−30 °C						
K equivalent	9.22E+12	9.76E+12	1.13E+13	1.01E+14	1.19E+14	2.45E+13
0.1 bar	0.62%	−2.44%	6.39%	−10.66%	−7.10%	−11.09%
0.5 bar	0.60%	−2.45%	6.39%	−10.66%	−7.10%	−11.24%
1 bar	0.54%	−2.45%	6.39%	−10.67%	−7.10%	−11.29%
5 bar	0.60%	−2.45%	6.39%	−10.66%	−7.09%	−11.41%
10 bar	0.54%	−2.45%	6.39%	−10.67%	−7.09%	−11.31%

with high relative roughness (4–6). The best results are obtained for the microchannels with lower relative roughness, independently of the peak density.

Approach 4. The final approach, which is also the one that gives the best results, consists in calculating the flow resistance of an equivalent smooth channel, not only with the same effective hydraulic diameter, but also with the same equivalent cross-sectional area, given by

$$d_h = \frac{4V_{fluid}}{A_{wet}} \qquad A = \frac{V_{fluid}}{L} \tag{18}$$

The procedure is repeated and the agreement at room temperature is very good (see Table 12), with errors below 6% for all models. At −30 °C, the differences are similar for the low roughness models and slightly higher for the high roughness models.

Logically, in real applications, the CFD technique cannot be used to model in detail the wall roughness, because, first, the detailed wall profile is unknown and second, the work necessary to build the detailed geometry and grid would be enormous. However, analytical expressions can be used to calculate the flow resistance value of the microchannels, from the values of the fluid volume and the wet surface. If the relative roughness is not very high, Approach 2 could be used, since some of the parameters that describe the wall roughness (ε, average peak height, RMS peak height, ...) can be experimentally measured.

4. Comparison with a 3D model

In order to analyse how realistic is the use of a 2D axisymmetric simplification for modelling roughness peaks in channels, a final model consisting of a rectangular 3D channel, in which the roughness peaks are modelled as pyramids, which are a more accurate representation of roughness peaks, has been built and its results compared with those of the 2D model.

Fig. 10 shows the geometry of the 3D microchannel that has been simulated and Table 13 shows its geometrical characteristics. The strategy that has been followed for the selection and modelling of the 3D channel and the subsequent comparison with the 2D model is the following: one of the 2D channels with high roughness values is selected (model 5) and a 3D rectangular channel with the same peak profile is built, using pyramids instead of 2D peaks. The height and width of the channel are adjusted so as to yield the same effective hydraulic diameter as model 5, using the definition of Approach 4 (Eq. (18)). Since the models should also have the same cross-sectional area, only a sector of the 2D model is considered for the comparison of results. In fact, in 2D axisymmetric models, the flow variables are solved in the 2D section that is modelled, and then extrapolated to the whole domain by multiplying the corresponding variables by $2 \cdot \pi$. Therefore, we can extrapolate the mass flow results of the complete 2D axisymmetric model to a sector of the same cross-sectional area as the 3D channel. For this extrapolation, either the

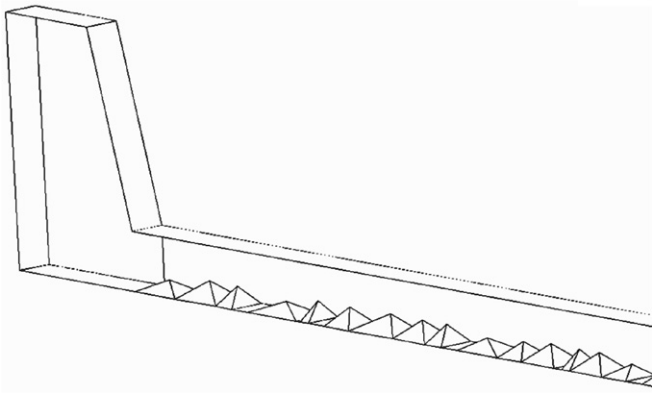

Fig. 10. Detail of the geometry of the 3D channel with pyramidal roughness peaks.

Table 13
Main characteristics of the 3D model and of model 5 (2D)

	Length (mm)	Height (μm)	Width (μm)	Fluid volume of channel (mm^3)	Wet surface of channel (mm^3)	Effective d_h (μm)	Cross-section at inlet (mm^2)	Sector of 2D model so that inlet cross-sections are equal (rad)	Effective cross-section (mm^2)	Sector of 2D model so that effective cross-sections are equal (rad)
2D	0.1	5	7E3	3.13E−2	15.79	7.94	3.49E−1	2.61E−4	3.13E−1	2.70E−4
3D	0.1	4.83	3	1.35E−6	6.78E−4	7.94	1.45E−5		1.35E−5	

Table 14
Comparison between the 2D and 3D models

ΔP_{BC}	Mass flow (gr/s) 3D model	Mass flow (gr/s) 2D model using sector of 2.61E−4 rad	Difference (%)	Mass flow (gr/s) 2D model using sector of 2.7E−4 rad	Difference (%)
1 bar	1.25E−6	1.22E−6	−2.65	1.26E−6	0.75
5 bar	6.25E−6	6.10E−6	−2.40	6.31E−6	1.01
10 bar	1.25E−5	1.22E−5	−2.65	1.26E−5	0.75

Table 15
Results of applying Approach 4 to the 3D model

ΔP_{BC}	$f \cdot Re$ (theory)	$f \cdot Re$ (CFD)	Difference CFD–theory (%)	Resistance coeff. K of 3D channel (CFD)	Resistance coeff. K of 3D channel using Approach 4	Difference (%)
1 bar	96	164	71	8.15E16	7.58E16	7.6
5 bar	96	164	71	8.14E16	7.58E16	7.5
10 bar	96	164	71	8.15E16	7.58E16	7.6

inlet cross-sectional area or the effective cross-sectional area, as defined in Eq. (18), can be used. More accurate results are obtained using the latter, as it will be shown below.

The fluid is the same brake oil used for the 2D simulation (see properties in Table 2). The domain is 3D with periodic boundary conditions at the side walls. The inlet and outlet pressure conditions are the same as those used in the 2D models.

The model is meshed with a very fine grid of 30 elements across the channel and a total of 610,500 cells. A much more refined mesh is also built, with twice the number of cells, and the mass flow results only change in 3%. Thus, no further refinements are performed, and the results of the refined mesh are used for the comparison.

The mass flow results are shown in Table 14. The difference between the results of the 2D and 3D model is below 1%, which indicates that the flow across the 2D roughness peaks is comparable to the flow across the 3D pyramids, that the approximation used for the studies conducted in the previous parts is valid and that the best equivalence between channels is the one described by Eq. (18). Moreover, Approach 4 can be applied to the 3D simulation. In case of flow between parallel plates, the Poiseuille number is, according to [26]

$$f \cdot Re = 96 \tag{19}$$

where, in this case, the hydraulic diameter used in the calculation of Re is defined as two times the height of the channel.

Table 15 shows the CFD results in terms of the Poiseuille number $f \cdot Re$ and the flow resistance coefficient K, the theoretical $f \cdot Re$ value of the smooth channel without peaks, and the flow coefficient K resulting from applying Approach 4. In accordance with the previously obtained results the inclusion of roughness significantly increases the Poiseuille number, and Approach 4, using an equivalent smooth channel with the same the effective hydraulic diameter and effective cross-sectional area, provides a good approximation to the real behaviour of the flow.

5. Conclusions

The influence of roughness on the laminar flow through very narrow and short annular channels, such as those that might appear in seal systems, has been investigated by means of numerical simulations, and a method has been proposed to analytically calculate the flow through these channels, based on the classical viscous flow equations. Wall roughness effects can be considered in the numerical models by modelling an equivalent smooth channel or in the analytical expressions by calculating the flow resistance of this equivalent smooth channel. The approach that yields the best results is to build a smooth channel with the same hydraulic diameter and cross-sectional area as the rough one, calculated from the fluid volume and the wet surface area. In the analytical models, secondary losses due to entrance, exit or developing flow must be taken into account, especially for $Re > 50$.

References

[1] J. Harley, H. Bau, Fluid flow in micron and submicron size channels, IEEE Trans. THO249 3 (1989) 25–28.

[2] X.F. Peng, G.P. Peterson, B.X. Wang, Friction flow characteristics of water flowing through microchannels, Exp. Heat Transfer 7 (1994) 249–283.

[3] X.N. Jiang, J.Y. Zhou, Y.L. Yao, X.Y. Ye, Micro-fluid flow in microchannel, Proc. Transducers 95 (1995) 317–320.

[4] D. Yu, R. Warrington, R. Barren, T. Ameel. An experimental and theoretical investigation of fluid flow and heat transfer in microtubes, in: Proceedings of the ASME/JSME Thermal Engineering Conference, ASME, vol. 1, 1995, pp. 523–530.

[5] G.M. Mala, D.Q. Li, C. Werner, H.J. Jacobasch, Y.B. Ning, Flow characteristics of water through a microchannel between two parallel plates with electrokinetic effects, Int. J. Heat Fluid Flow 18 (1997) 489–496.

[6] I. Papautsky, J. Brazzle, T. Ameel, A.B. Frazier, Laminar fluid behavior in microchannels using micropolar fluid theory, Sens. Actuators, A 73 (1999) 101–108.

[7] I. Papautsky, T.A. Ameel, B.K. Gale, S. Mohanty, A.B. Frazier, Effects of rectangular microchannel aspect ratio on laminar friction constant, SPIE 3877 (1999) 147–158.

[8] G.M. Mala, D.Q. Li, Flow characteristics of water in microtubes, Int. J. Heat Fluid Flow 20 (1999) 142–148.

[9] D. Pfund, D. Rector, A. Shekarriz, A. Popescu, J. Welty, Pressure drop measurements in a microchannel, AICHE J. 46 (2000) 1496–1507.

[10] W.L. Qu, G.M. Mala, D.Q. Li, Pressure driven water flows in trapezoidal silicon microchannels, Int. J. Heat Mass Transfer 43 (2000) 353–364.

[11] L.Q. Ren, W.L. Qu, D.Q. Li, Interfacial electrokinetic effects on liquid flow in microchannels, Int. J. Heat Mass Transfer 44 (2001) 3125–3134.

[12] I. Papautsky, T. Ameel, A . B. Frazier, A review of laminar single phase flow in microchannels, in: Proceedings of 2001 ASME International Mechanical Engineering Congress and Exposition, NY, 11–16 November 2001, pp. 495–503.

[13] S.M. Flockhart, R.S. Dhariwal, Experimental and numerical investigation into the flow characteristics of channels, J. Fluids Eng. 120 (1998) 291–295.

[14] B. Xu, K.T. Ooi, N.T. Wong, W.K. Choi, Experimental investigation of flow friction for liquid flow in microchannels, Int. Commun. Heat Mass Transfer 27 (2000) 1165–1176.

[15] H.H. Bau, J.N. Pfahler, Experimental observations of liquid flow in micro conduits, in: Proceedings of 39th AIAA Aerospace Science Meeting and Exhibit, Reno, NV, 8–11 January 2001, AIAA paper 2001-0722.

[16] J. Judy, D. Maynes, B.W. Webb, Characterization of frictional pressure drop for liquid flows through microchannels, Int. J. Heat Mass Transfer 45 (2002) 3477–3489.

[17] D. Liu, S.V. Garimella, Investigations of liquid flow in microchannels, AIAA J. Thermophys. Heat Transfer 18 (2004) 65–72.

[18] H.Y. Wu, P. Cheng, Friction factors in smooth trapezoidal silicon microchannels with different aspect ratios, Int. J. Heat Transfer 46 (2003) 2519–2525.

[19] M.J. Kohl, S.I. Abdel-Khalik, S.M. Jeter, D.L. Sadowski, An experimental investigation of microchannel flow with internal pressure measurements, Int. J. Heat Mass Transfer 48 (8) (2005) 1518–1533.

[20] K.C. Toh, X.Y. Chen, J.C. Chai, Numerical computation of fluid flow and heat transfer in microchannels, Int. J. Heat Mass Transfer 45 (2002) 5133–5141.

[21] P.S. Lee, S.V. Garimella, D. Liu, Investigation of heat transfer in rectangular microchannels, Int. J. Heat Mass Transfer 48 (9) (2005) 1688–1704.

[22] W. Qu, I. Mudawar, Experimental and numerical study of pressure drop and heat transfer in a single phase microchannel heat sink, Int. J. Heat Mass Transfer 45 (2002) 2549–2565.

[23] J. Yue, G. Chen, Q. Yuan, Pressure drops of single and two-phase flows through T-type microchannel mixers, Chem. Eng. J. 102 (2004) 11–24.

[24] W. Yang, J. Zhang, H. Chen, The study of flow characteristics of curved microchannels, Appl. Therm. Eng. 25 (13) (2005) 1894–1907.

[25] G. Croce, P. D'Agaro, Numerical analysis of roughness effect on microtube heat transfer, Superlattices Microstruct. 35 (2004) 601–616.

[26] F. White, Fluid Mechanics, McGraw-Hill, 1979, chapter 6.

[27] Fluent Inc., Fluent Users Guide, Cavendish, Lebanon NH, USA, 2005.

[28] S.V. Patankar, Numerical Heat Transfer and Fluid Flow, Hemisphere, Washington, DC, 1980.

[29] S.R. Mathur, J.Y. Murthy, A pressure-based method for unstructured meshes, Numer. Heat Transfer 31 (1997) 195–215.

[30] S.E. Kim, S.R. Mathur, J.Y. Murthy, D. Choudhury, A Reynolds-Averaged Navier Stokes Solver Using Unstructured Mesh-Based Finite Volume Scheme, AIAA-Paper 98-0231, 1998.

[31] P. Dooley, S.L. Bernasek, Pooling analysis of scanning probe microscopy images, Surf. Sci. 406 (1998) 206–220.